Nanofibers Comprising Yolk–Shell Sn@void@SnO/SnO_2 and Hollow SnO/SnO_2 and SnO_2 Nanospheres via the Kirkendall Diffusion Effect and Their Electrochemical Properties

*Jung Sang Cho and Yun Chan Kang**

Nanofibers with a unique structure comprising Sn@void@SnO/SnO_2 yolk–shell nanospheres and hollow SnO/SnO_2 and SnO_2 nanospheres are prepared by applying the nanoscale Kirkendall diffusion process in conventional electrospinning process. Under a reducing atmosphere, post-treatment of tin 2-ethylhexanoate-polyvinylpyrrolidone electrospun nanofibers produce carbon nanofibers with embedded spherical Sn nanopowders. The Sn nanopowders are linearly aligned along the carbon nanofiber axis without aggregation of the nanopowders. Under an air atmosphere, oxidation of the Sn–C composite nanofibers produce nanofibers comprising Sn@void@SnO/SnO_2 yolk–shell nanospheres and hollow SnO/SnO_2 and SnO_2 nanospheres, depending on the post-treatment temperature. The mean sizes of the hollow nanospheres embedded within tin oxide nanofibers post-treated at 500 °C and 600 °C are 146 and 117 nm, respectively. For the 250th cycle, the discharge capacities of the nanofibers prepared by the nanoscale Kirkendall diffusion process post-treated at 400 °C, 500 °C, and 600 °C at a high current density of 2 A g^{-1} are 663, 630, and 567 mA h g^{-1}, respectively. The corresponding capacity retentions are 77%, 84%, and 78%, as calculated from the second cycle. The nanofibers prepared by applying the nanoscale Kirkendall diffusion process exhibit superior electrochemical properties compared with those of the porous-structured SnO_2 nanofibers prepared by the conventional post-treatment process.

1. Introduction

Nanostructured tin dioxide (SnO_2) materials with a wide bandgap of 3.54 eV are widely used in various fields such as gas sensing, catalysts, and energy storage.[1–36,39,40] In particular, SnO_2 materials with a specific nanostructure featuring both a short Li^+ ion diffusion length and sufficient void space to accommodate the volume change during cycling have been developed by liquid solution and gas phase reaction processes for applications in lithium ion batteries (LIBs). The developed structures include nanotubes,[1–7] nanowires,[8–10] fiber-in-tubes,[12] nanoboxes,[18] hollow cubes,[13] bowl-like-structures,[14] core–shells,[26–29] yolk–shells,[19] 3DOM-structures,[15] and flower-shaped[24] structures. Hollow SnO_2 nanostructures have been explored as a suitable structure for the design of new LIB electrodes because of their improved cycling abilities and rate capabilities.[3–8,13,29–35] Li et al. synthesized hollow SnO_2 nanospheres by calcining PS@SnO_2 core–shell spheres prepared through the sol–gel process.[28] By modifying the experimental parameters, hollow SnO_2

J. S. Cho, Prof. Y. C. Kang
Department of Materials Science and Engineering
Korea University, Anam-Dong
Seongbuk-Gu, Seoul 136-713, Republic of Korea
E-mail: yckang@korea.ac.kr

DOI: 10.1002/smll.201500940

spheres with tunable morphologies and properties were produced, which exhibited sufficiently high activity for use as an anode material for LIBs. Ye et al. prepared SnO_2 nanotubes with controllable morphologies using a 1D silica mesostructure as a sacrificial template via a simple hydrothermal route.[3] The obtained SnO_2 nanotubes performed well as an anode material within LIBs. Lou and co-workers demonstrated a facile method for the rapid formation of SnO_2 nanoboxes with uniform morphology, good structural stability, and a tunable interior volume via template-engaged coordinating etching of pregrown Cu_2O nanocubes at room temperature.[18] The obtained SnO_2 nanoboxes exhibited a high lithium storage capacity and an excellent cycling performance.

In general, novel self-templated methods such as those based on the nanoscale Kirkendall effect, Ostwald ripening, galvanic replacement, and surface-protected etching are advantageous compared to the above template-dependent methods in terms of the scalability, cost, and simplicity of the synthetic procedures.[33–38] Wang and co-workers developed hierarchical hollow SnO_2 nanostructures synthesized via a simple template-free hydrothermal method using tin sulfate as the precursor.[36] Owing to SnO_2 nanospheres and a hollow interior, the unique mesoporous shell showed high capacities and excellent cycling performances as anode materials for LIBs.

Electrospinning is a powerful technique that is used for the fabrication of inorganic hollow nanofibers. Both the use of templates and coelectrospinning technique have been applied to form hollow SnO_2 nanofibers.[5–7,10–12] The Ostwald ripening effect has also been applied for the preparation of hollow SnO_2 nanofibers.[4] However, to the best of our knowledge, the nanoscale Kirkendall diffusion process has not been applied for the preparation of SnO_2 nanofibers via an electrospinning process.

In this study, we propose for the first time novel-structured nanofibers composed of yolk–shell nanospheres were prepared by applying the nanoscale Kirkendall diffusion process to the conventional electrospinning process. Nanofibers composed of Sn@void@SnO/SnO_2 yolk–shell nanospheres and hollow SnO/SnO_2 nanospheres were prepared by controlling the post-treatment temperatures of the electrospun nanofibers. The key concept for the preparation of these SnO_2 nanofibers involved the formation of Sn–C composite nanofibers with a uniform distribution of nonaggregated spherical Sn nanopowders within an amorphous carbon nanofiber as an intermediate product. The electrochemical properties of the nanofibers composed of Sn@void@SnO/SnO_2 yolk–shell nanospheres and hollow SnO/SnO_2 and SnO_2 nanospheres were compared with those of the porous-structured SnO_2 nanofibers, as an anode material for LIBs.

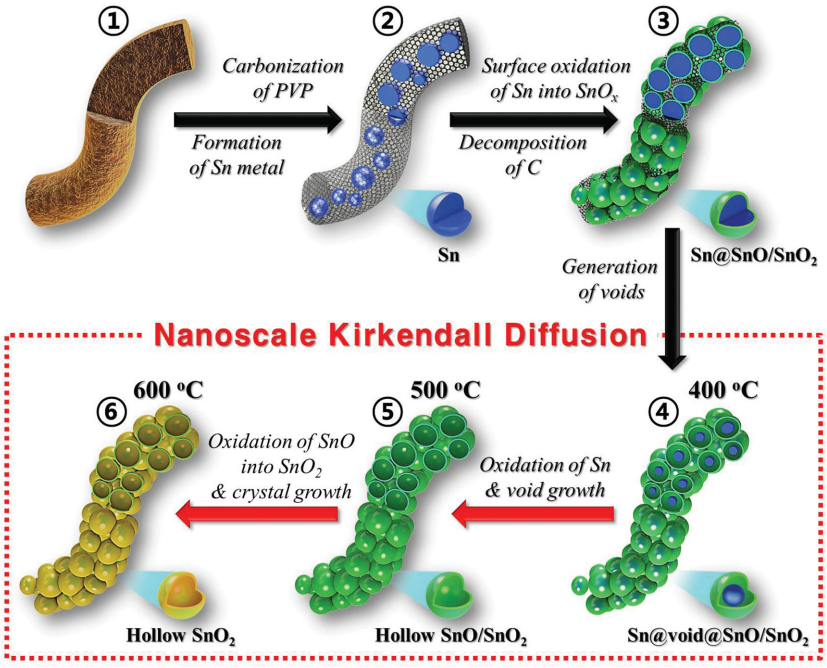

Scheme 1. Formation scheme of the nanofibers composed of Sn@void@SnO/SnO_2 yolk–shell nanospheres and hollow SnO/SnO_2 and SnO_2 nanospheres.

2. Results and Discussion

Nanofibers composed of Sn@void@SnO/SnO_2 yolk–shell nanospheres and hollow SnO/SnO_2 and SnO_2 nanospheres were prepared by applying a two-step post-treatment process to the electrospun nanofibers. The formation mechanism for the three types of nanofibers is described in **Scheme 1**. Under a reducing atmosphere, the post-treatment of the $Sn(Oct)_2$-PVP nanofibers formed by the electrospinning process produced carbon nanofibers with embedded spherical Sn nanopowders. The Sn nanopowders were linearly aligned along the axis of the carbon nanofiber without the aggregation of the nanopowders. During the reduction process, the amorphous carbon minimized the crystal growth of the Sn metal during the long period required for the complete reduction of SnO_x into Sn metal. Under an air atmosphere, the oxidation of the Sn–C composite nanofibers produced nanofibers composed of Sn@void@SnO/SnO_2 yolk–shell nanospheres and hollow SnO/SnO_2 and SnO_2 nanospheres, depending on the post-treatment temperatures. The nanoscale Kirkendall diffusion process that occurred during the oxidation of the Sn–C composite nanofibers transformed the spherical Sn nanopowders into hollow SnO_2 nanospheres. The surface oxidation of the Sn nanopowders formed a Sn/SnO core–shell structure, as described in **Scheme 2**. The Sn cations diffused outwards more rapidly than the inward diffusion of oxygen; this is consistent with the larger ionic radius of O^{2-} anions (140 pm) compared to that of Sn cations (Sn^{2+} is 93 pm, Sn^{4+} is 69 pm). Further oxidation transformed SnO into SnO_2 during the nanoscale Kirkendall diffusion process. At an oxidation temperature of 400 °C, the Sn nanopowder transformed into the Sn-SnO-SnO_2 yolk–shell nanopowder with a configuration of Sn@void@SnO/SnO_2. At 400 °C, the Sn nanopowder did not completely transform into hollow

small NANO MICRO

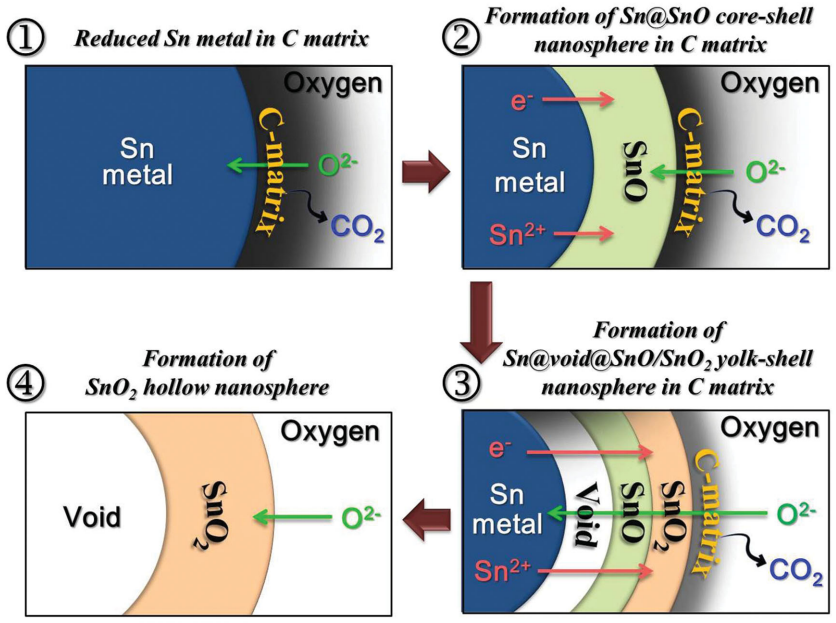

Scheme 2. Formation mechanism of a hollow SnO_2 nanosphere in the nanofiber by the nanoscale Kirkendall diffusion effect and its chemical conversion process in the surface region of a sphere.

SnO_2 nanospheres via the nanoscale Kirkendall diffusion process within the short oxidation period of 2 h. However, at oxidation temperatures of 500 °C and 600 °C, the complete conversion of Sn metal into tin oxide nanospheres via the nanoscale Kirkendall diffusion resulted in the formation of hollow SnO/SnO_2 and SnO_2 nanospheres, respectively. In addition, during the oxidation process, the amorphous carbon decomposed into CO_2 gas, resulting in the necking between the hollow SnO_2 nanospheres, as described in Scheme 1. Consequently, the SnO_2 nanofibers composed of loosely connected hollow SnO_2 nanospheres were prepared at an oxidation temperature of 600 °C.

The formation mechanism of the SnO_2 nanofibers that consisted of loosely connected hollow SnO_2 nanospheres was investigated on the basis of post-treatment-induced morphology changes in the electrospun precursor nanofibers at various temperatures. The morphologies of the Sn–C nanofibers obtained by the reduction of the electrospun nanofibers at of 400 °C under 10% H_2/Ar gas are shown in **Figure 1**. The nanofibers observed in the transmission electron microscopy (TEM) and scanning electron microscopy (SEM) images exhibited a salamander egg-like structure. The Sn nanopowders that exhibit white and black colors in the SEM and TEM images, respectively, are linearly aligned along the translucent carbon nanofiber without the aggregation of the nanopowders. During the early stage of the reduction process, the carbonization of the PVP and the decomposition of $Sn(Oct)_2$ resulted in the formation of the SnO_x–C composite nanofibers with a homogeneous morphology as an intermediate product. The reduction of SnO_x into Sn metal and the subsequent segregation resulted in aggregation-free Sn nanopowders uniformly aligned within the amorphous carbon nanofiber. The mean size of the Sn metal nanopowders was 120 nm, as measured from the TEM images. The X-ray diffractometry (XRD) pattern of the nanofibers obtained by the reduction process exhibited a pure-phase metallic Sn crystal structure, as shown in Figure 1d. The line profiling and elemental mapping images revealed the pure Sn metal nanopowder embedded within the carbon layer, as shown in Figure 1e,f. The thick carbon layer disrupted the surface oxidation of the Sn metal nanopowder.

The Sn–C nanofibers were post-treated at 400 °C, 500 °C, and 600 °C under an air atmosphere. The crystal peaks of metallic Sn were observed in the XRD pattern of the nanofibers post-treated at 400 °C under an air atmosphere, as shown in Figure S1 (Supporting Information). The complete conversion of metallic Sn into SnO or SnO_2 did not occur at a post-treatment temperature of 400 °C(conducted for 2 h). Nanofibers post-treated at 500 °C under an air atmosphere exhibited a mixed crystal structure comprising SnO and SnO_2 phases. However, nanofibers post-treated at 600 °C under an air atmosphere exhibited a pure crystal structure of cubic SnO_2. The results of the XRD patterns shown in Figure S1 (Supporting Information) revealed that the oxidation of the Sn metal via the nanoscale Kirkendall diffusion process initially formed a SnO phase. The SnO nanocrystals transformed into the SnO_2 nanocrystals through a further oxidation process. By applying the Scherrer equation to the (110) cubic SnO_2 peak, the mean crystallite sizes of the nanofibers post-treated at 400 °C, 500 °C, and 600 °C under an air atmosphere were calculated to be 22, 36, and 43 nm, respectively. The morphological changes of the Sn–C nanofibers according to the oxidation temperatures are shown in **Figures 2–4**. The morphologies of the nanofibers post-treated at 400 °C under an air atmosphere are shown in Figure 2. The translucent amorphous carbon was not observed in the SEM and TEM images of the nanofibers. During the reduction process, the segregation of metallic Sn into the nanopowders resulted in the formation of translucent amorphous carbon with a porous structure. Therefore, complete decomposition of amorphous carbon into CO_2 gas occurred even at a low oxidation temperature of 400 °C under an air atmosphere. The contraction of the nanofibers during carbon decomposition and the growth of the nanopowders via the nanoscale Kirkendall diffusion process resulted in the formation of connections between the nanopowders. Therefore, nanofibers consisting of loosely connected nanopowders were obtained after the post-treatment under an air atmosphere, as shown by the SEM and TEM images in Figure 2a,b, respectively. The high-resolution TEM images shown in Figure 2c,d revealed the detailed structure of the nanofibers. The nanopowders embedded within the nanofibers exhibited a clear yolk–shell structure. A clear void was observed between the core and shell components of the nanopowders formed by the nanoscale Kirkendall diffusion process, as shown by the arrows in Figure 2. Incomplete

www.MaterialsViews.com

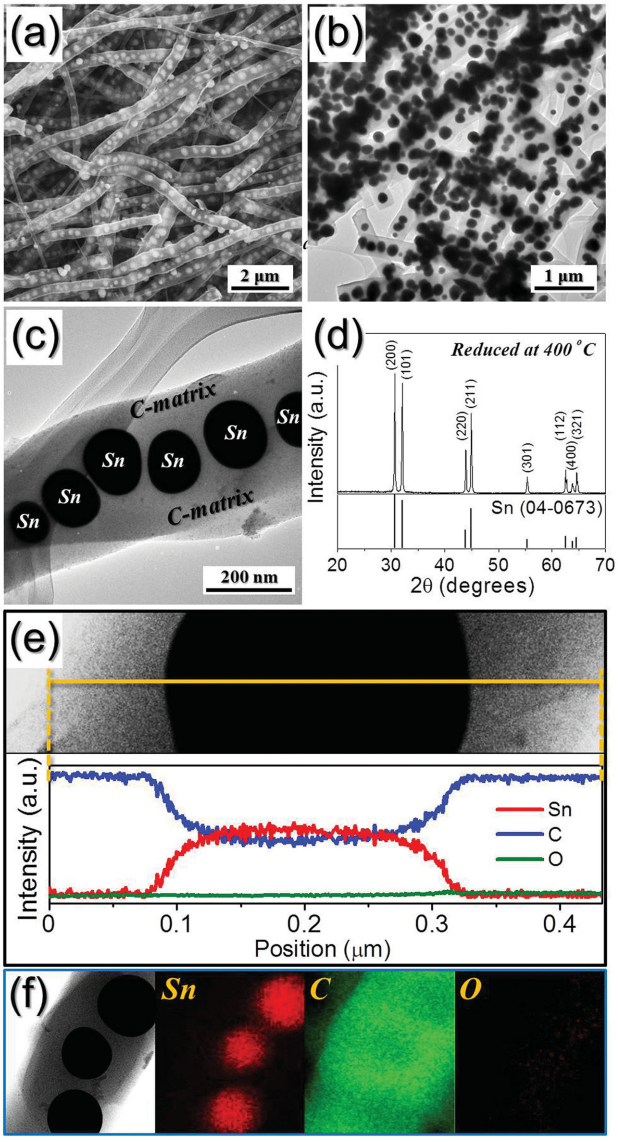

Figure 1. Morphologies, XRD pattern, line profiling analysis, and elemental mapping images of the Sn–C nanofibers obtained by reduction process of as-spun $Sn(Oct)_2$–PVP composite nanofibers at 400 °C under 10% H_2/Ar gas: a) SEM, b,c) TEM images, d) XRD pattern, e) line profiling analysis, and f) elemental mapping images.

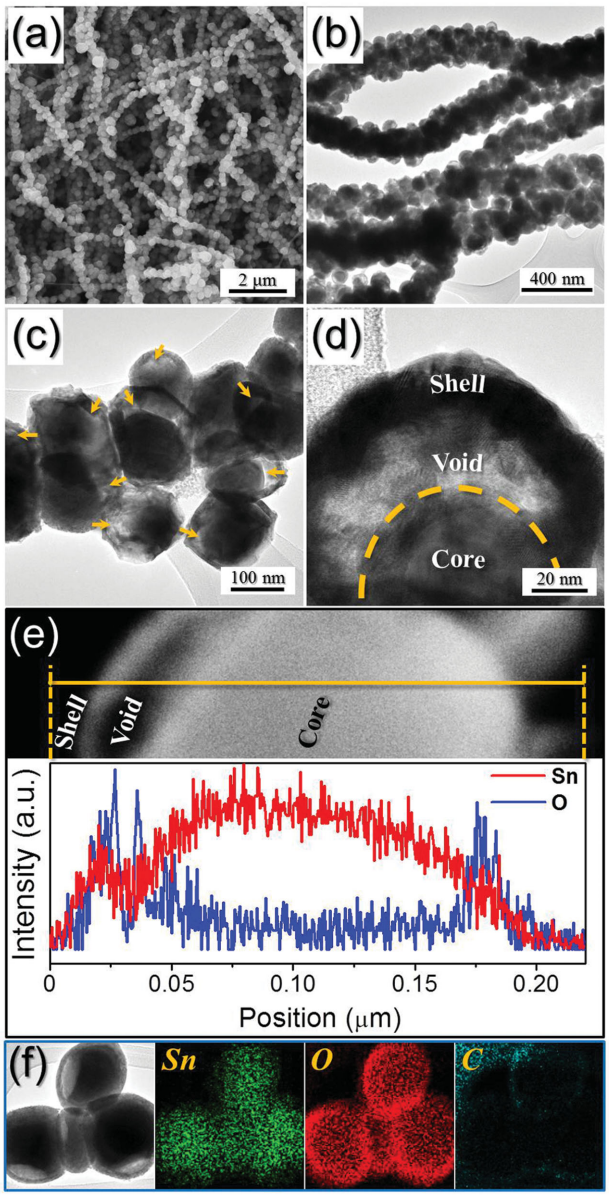

Figure 2. Morphologies, line profiling analysis, and elemental mapping images of the nanofibers composed with Sn@void@SnO/SnO_2 yolk–shell nanospheres obtained by oxidation of reduced Sn–C composite nanofibers at 400 °C under air: a) SEM, b–d) TEM images, e) line profiling analysis, and f) elemental mapping images.

conversion of metallic Sn into SnO/SnO_2 by the nanoscale Kirkendall diffusion process resulted in yolk–shell structured nanopowders. The XRD pattern shown in Figure S1 (Supporting Information) also revealed incomplete conversion of metallic Sn into SnO/SnO_2. Deconvolution of XPS Sn 3d peaks at binding energies of 484.9 eV (Sn $3d_{5/2}$) and 493.2 eV (Sn $3d_{3/2}$) also confirmed the presence of metallic Sn, as shown in Figure S2 (Supporting Information). Consequently, the nanopowders exhibited a yolk–shell structure with a configuration of Sn@void@SnO/SnO_2, as demonstrated in Figure 2c,d. The line profiling and elemental mapping images also revealed the clear configuration of Sn@void@SnO/SnO_2, as demonstrated in Figure 2e,f. The elemental mapping images and thermogravimetric (TG) curve shown in Figure 2f and S3, Supporting Information, respectively, revealed that the post-treatment at 400 °C under an air atmosphere formed carbon-free nanofibers. The size of the core and the thickness of the shell of the yolk–shell nanopowder were 83 and 12 nm, respectively, as shown in Figure 2d.

The morphologies of the nanofibers consisting of tin oxide hollow nanospheres post-treated at 500 °C and 600 °C under an air atmosphere are shown in Figures 3 and 4, respectively. The SEM and low-resolution TEM images of the nanofibers post-treated at 500 °C and 600 °C exhibited a similar structure. The nanofibers post-treated at 500 °C and 600 °C consisted of nanopowders composed of hollow nanospheres. The hollow nanospheres resulted from the complete conversion of metallic Sn into tin oxide via the nanoscale Kirkendall diffusion process. Evidence for the oxidation of Sn into SnO_x was further supported by observing only the

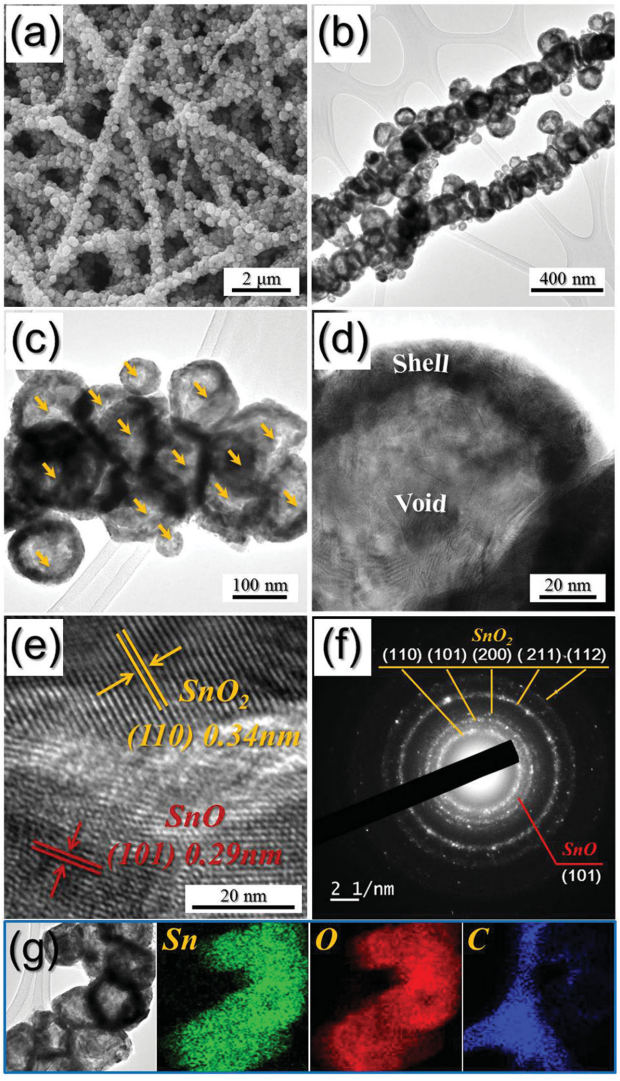

Figure 3. Morphologies, SAED pattern, and elemental mapping images of the nanofibers composed with hollow SnO/SnO_2 nanospheres obtained by oxidation of reduced Sn–C composite nanofibers at 500 °C under air: a) SEM, b–d) TEM images, e) HR-TEM image, f) SAED pattern, and g) elemental mapping images.

Sn peaks for the oxides with binding energies of 486.6 eV ($Sn\ 3d_{5/2}$) and 493.31 eV ($Sn\ 3d_{3/2}$) within the XPS spectra, as shown in Figure S2 (Supporting Information). The mean sizes of the hollow nanospheres within the nanofibers post-treated at 500 °C and 600 °C were 146 and 123 nm, respectively, as measured from the TEM images. Through the nanoscale Kirkendall diffusion process, the size of the nanopowders increased from 120 to 146 nm at a post-treatment temperature of 500 °C. However, densification and sintering occurred at a high post-treatment temperature of 600 °C, and this slightly decreased the mean size of the hollow SnO_2 nanospheres. The high-resolution TEM images revealed different morphologies of the nanopowders within the nanofibers post-treated at 500 °C and 600 °C. The hollow tin oxide nanospheres exhibited smooth rounded surfaces, as shown in Figure 3d. However, the hollow SnO_2 nanosphere exhibited a well-faceted crystal structure, as observed by the high-resolution TEM image in Figure 4d. The thicknesses of the shells of the hollow tin oxide nanospheres were 12 and 15 nm, as shown in Figures 3d and 4d, respectively. The enlarged TEM images demonstrated that the clear lattice fringes were separated by 0.34 nm; this corresponds to the (110) lattice plane of cubic SnO_2, as shown in Figures 3e and 4e. The clear lattice fringes were separated by 0.29 nm (Figure 3e); this corresponds to the (101) lattice plane of SnO. The selected area electron diffraction (SAED) pattern of the nanofibers revealed the highly crystalline structure of the tin oxide nanofibers post-treated at 500 °C and 600 °C, as shown in Figures 3f and 4f. The elemental mapping images of the nanofibers post-treated at 500 °C and 600 °C under an air atmosphere showed a trace amount of the carbon component, as shown in Figures 3g and 4g. The TG curve also revealed that the post-treatment at 500 °C and 600 °C under an air atmosphere formed carbon-free nanofibers composed of hollow tin oxide nanospheres, as shown in Figure S3 (Supporting Informa-

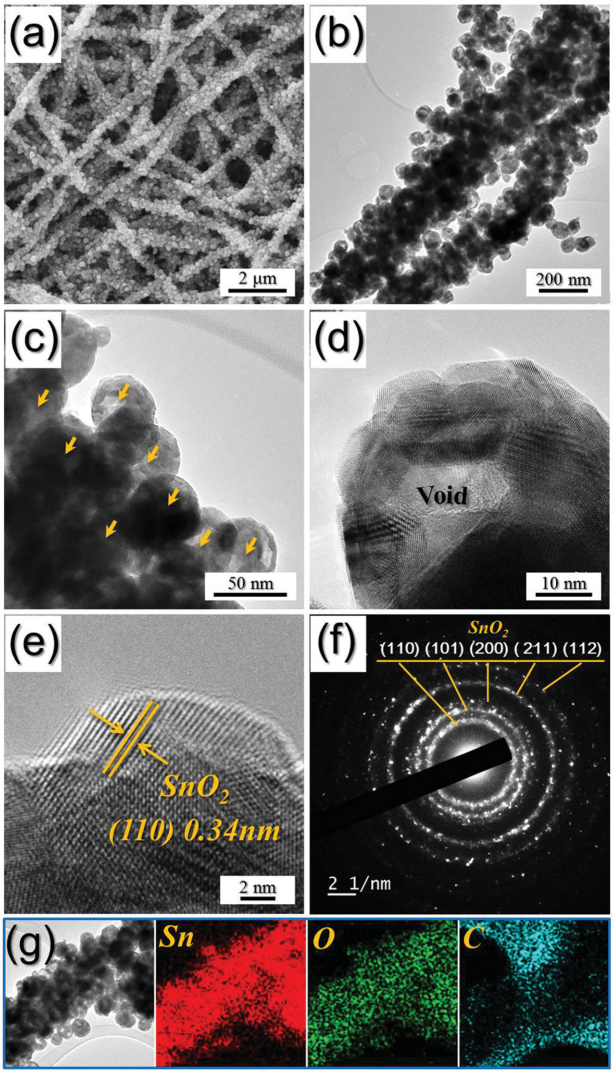

Figure 4. Morphologies, SAED pattern, and elemental mapping images of the nanofibers composed with hollow SnO_2 nanospheres obtained by oxidation of reduced Sn–C composite nanofibers at 600 °C under air: a) SEM, b–d) TEM images, e) HR-TEM image, f) SAED pattern, and g) elemental mapping images.

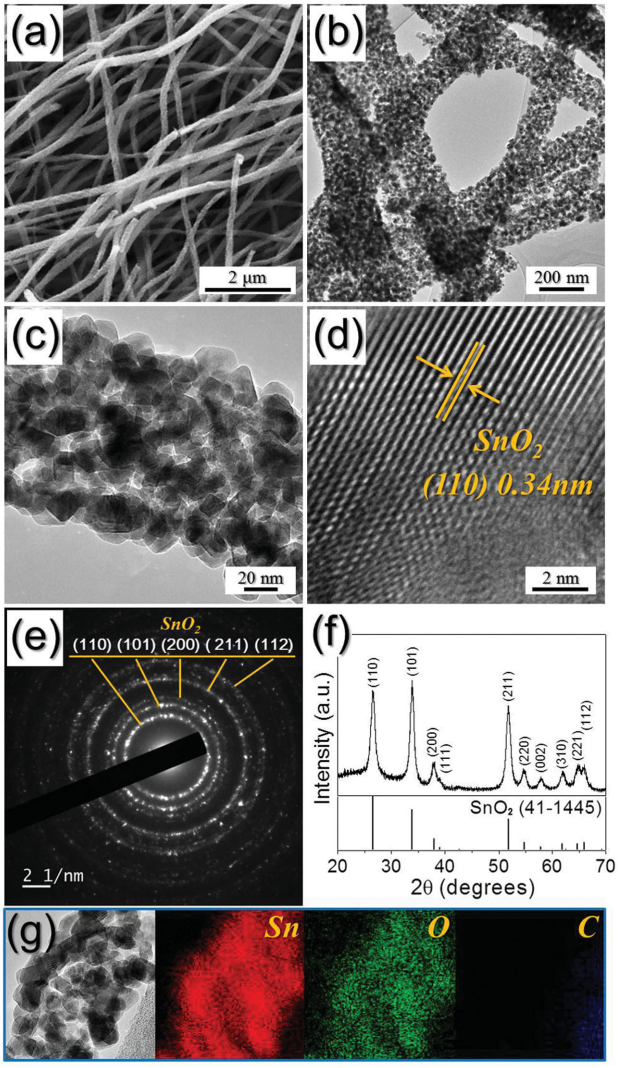

Figure 5. Morphologies, SAED pattern, XRD pattern, and elemental mapping images of the porous SnO_2 nanofibers obtained by direct oxidation of as-spun $Sn(Oct)_2$–PVP composite nanofibers at 500 °C under air: a) SEM, b) and c) TEM images, d) HR-TEM image, e) SAED pattern, f) XRD pattern, and g) elemental mapping images.

tion). The Brunauer-Emmett-Teller (BET) surface areas of the tin oxide nanofibers post-treated at 400 °C, 500 °C, and 600 °C were 11.5, 9.2, and 3.4 $m^2\ g^{-1}$, respectively (Figure S4, Supporting Information).

The characteristics of the SnO_2 nanofibers prepared by the conventional post-treatment process of the electrospun nanofibers are demonstrated in **Figure 5**. The electrospun nanofibers were post-treated at 500 °C for 2 h under an air atmosphere. The overall structure of the nanofibers was retained even after the post-treatment under an air atmosphere, as shown by the SEM and low-resolution TEM images shown in Figure 5a–c. The TEM images shown in Figure 5b,c revealed the porous structure of the SnO_2 nanofibers, in which ultrafine nanocrystals of less than 20 nm in size were adhered together. The high-resolution TEM image, SAED pattern, and XRD pattern revealed the formation of highly crystalline SnO_2 nanofibers, as demonstrated in Figure 5d–f. The complete combustion of the carbon material produced carbon-free SnO_2 nanofibers, as confirmed by the elemental mapping images in Figure 5g. The mean crystallite size and BET surface area of the porous-structured SnO_2 nanofibers were 13 nm and 30.1 $m^2\ g^{-1}$, respectively.

The electrochemical properties of the tin oxide nanofibers formed via the nanoscale Kirkendall diffusion process were compared with those of the porous-structured SnO_2 nanofibers formed by a conventional post-treatment process. The first five cycles of the cyclic voltammogram (CV) curves of the nanofibers consisting of Sn@void@SnO/SnO_2 yolk–shell nanospheres are shown in **Figure 6**a; the scan rate was set as 0.07 mV s^{-1}. During the first cathodic step, an apparent reduction peak was observed at approximately 0.8 V. This was mainly associated with the formation of both metallic Sn nanograins and amorphous Li_2O through the reduction of SnO and SnO_2.[9] The broad reduction peak at approximately

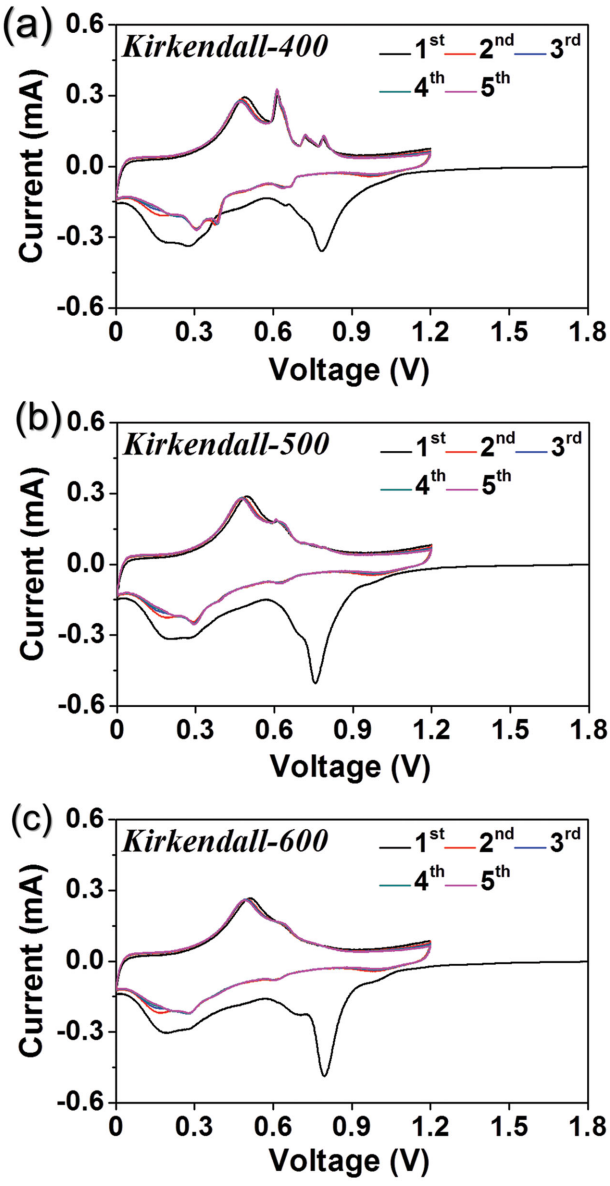

Figure 6. Cyclic voltammogram (CV) curves of the tin oxide nanofibers formed by applying the nanoscale Kirkendall diffusion process at different temperatures for the first five cycles at a scan rate of 0.07 mV s^{-1}.

0.2 V was attributed to the alloying reaction between Li and Sn, which formed Li_xSn alloys.[41,42] The oxidation peaks observed between 0.25 and 0.8 V during the first anodic scan were associated with the dealloying reaction of the Li_xSn alloys.[22] From the second cycle onwards, the decomposition peaks of SnO and SnO_2 at approximately 0.8 V disappeared, and the related peaks of the Li–Sn alloying and dealloying reactions were repeatedly presented. The CV curves of the nanofibers prepared by the application of the nanoscale Kirkendall diffusion process at post-treatment temperatures of 500 °C and 600 °C are shown in Figure 6b,c, respectively. The relative intensities of the reduction peaks observed at approximately 0.8 V in Figure 6b,c were higher than those observed in Figure 6a. The shapes of the CV curves changed with the different crystal structures of the nanofibers, depending on the post-treatment temperatures. The small amount of tin oxide within the nanofibers prepared by applying the nanoscale Kirkendall diffusion process at a post-treatment temperature of 400 °C resulted in a low-intensity reduction peak observed at approximately 0.8 V. The satisfactory overlapping of the CV curves from the second cycle onwards revealed good reversibility of the electrochemical reactions in the tin oxide nanofibers prepared by applying the nanoscale Kirkendall diffusion process.

The initial charge and discharge curves of the tin oxide nanofibers at a constant current density of 2 A g^{-1} are shown in **Figure 7**a. All the tin oxide nanofibers exhibited similarly shaped initial discharge curves, irrespective of their morphologies and compositions. The four samples also exhibited similar initial discharge capacities of approximately 1750 mA h g^{-1}. However, the nanofibers consisting of the Sn@void@SnO/SnO_2 yolk–shell nanospheres exhibited the highest initial charge capacity of 816 mA h g^{-1}. The Sn material exhibited a lower initial irreversible capacity loss than the SnO and SnO_2 materials. As a result, the nanofibers composed of the Sn@void@SnO/SnO_2 yolk–shell nanospheres exhibited the highest initial Coulombic efficiency. The initial Coulombic efficiencies of the nanofibers were 47%, 43%, 42%, and 35% for the Kirkendall-400, Kirkendall-500, Kirkendall-600, and porous SnO_2 nanofiber samples. The cycling performances of the four samples at a high current density of 2 A g^{-1} are shown in Figure 7b. For the 250th cycle, the discharge capacities of the nanofibers prepared by applying the nanoscale Kirkendall diffusion process at post-treatment temperatures of 400 °C, 500 °C, and 600 °C were 663, 630, and 567 mA h g^{-1}, respectively, and their corresponding capacity retentions were 77%, 84%, and 78%, as calculated from the second cycle. The second and 250th discharge capacities of the porous SnO_2 nanofibers formed by the conventional post-treatment process were 604 and 381 mA h g^{-1}, and their capacity retention was 63%, as calculated from the second cycle. The rate performances of the nanofibers prepared by the nanoscale Kirkendall diffusion process were compared with those of the nanofibers prepared by the conventional post-treatment process, as shown in Figure 7c. It can be observed that the current density increased progressively from 0.5 to 8.0 A g^{-1}, with 10 cycles being performed at each step. The nanofibers exhibited good rate performances irrespective of the post-treatment conditions.

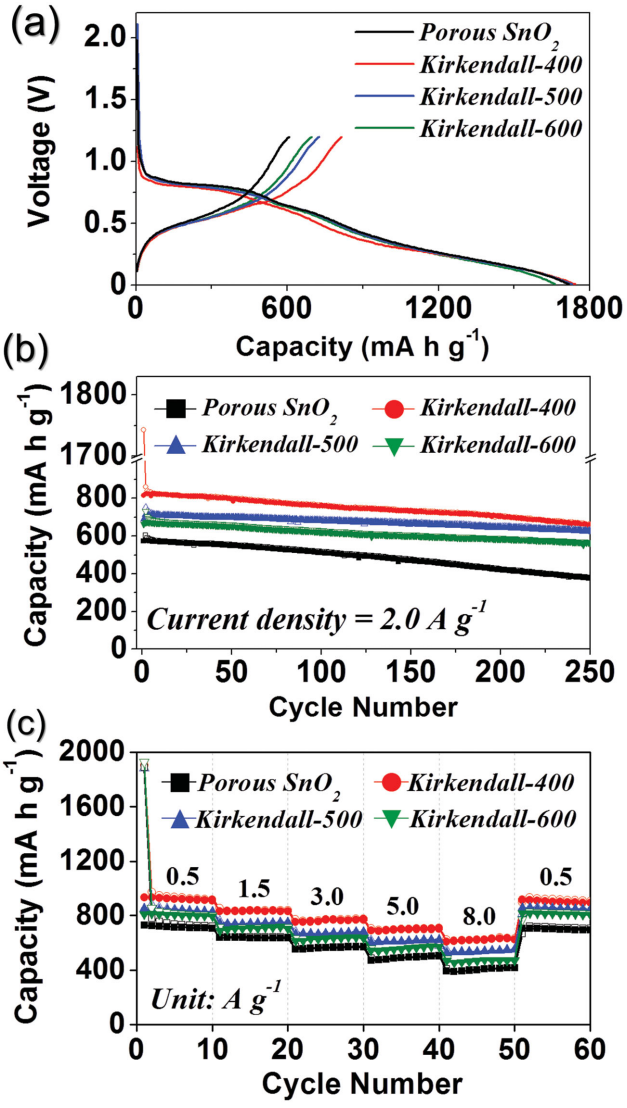

Figure 7. Electrochemical properties of the tin oxide nanofibers formed by applying the nanoscale Kirkendall diffusion process and porous-structured SnO_2 nanofibers formed by conventional post-treatment process: a) initial charge/discharge curves at a constant current density of 2.0 A g^{-1}, b) cycle performances at a constant current density of 2.0 A g^{-1}, and c) rate performances.

The final rate capacities of the tin oxide nanofibers prepared by applying the nanoscale Kirkendall diffusion process at a post-treatment temperature of 500 °C were 829, 750, 682, 581, and 553 mA h g^{-1} at current densities of 0.5, 1.5, 3.0, 5.0, and 8.0 A g^{-1}, respectively. Following 50 cycles, the discharge capacity of the tin oxide nanofibers recovered well to 863 mA h g^{-1} as the current density returned to 0.5 A g^{-1}.

The impedance spectra of the nanofibers prepared by applying the nanoscale Kirkendall diffusion process were compared with those of the nanofibers prepared by the conventional post-treatment process prior to and following the cycling, as shown in Figures S5 and S6, Supporting Information. The impedance measurements were conducted at room temperature on the cells containing the nanofibers prior to and following 10 and 50 cycles in the potential range 0.01–1.2 V at a current density of 2.0 A g^{-1}. The impedance

spectra exhibited a semicircle and an inclined line. The semicircle within the medium-frequency range of the impedance spectrum was assigned to the charge-transfer resistance (R_{ct}) of the electrode used in the measurements.[19,43,44] Prior to cycling, the porous-structured tin oxide nanofibers prepared by the conventional post-treatment process exhibited a lower charge-transfer resistance than that of the nanofibers prepared by applying the nanoscale Kirkendall diffusion process, as shown in Figure S5 (Supporting Information). Furthermore, the opposite result was observed following 10 and 50 cycles, as shown in Figure S6 (Supporting Information). The morphologies of the nanofibers formed by applying the nanoscale Kirkendall diffusion process and porous-structured SnO_2 nanofibers formed by conventional post-treatment process obtained after 50 cycles are shown in Figure S7 (Supporting Information). The nanofibers (Kirkendall-400 and Kirkendall-500) composed of hollow tin oxide nanospheres formed by applying the nanoscale Kirkendall diffusion process maintained their morphologies even after repeated lithium insertion and desertion processes as shown by TEM images in Figure 7Sa–f, Supporting Information. However, the structure of SnO_2 nanofiber with porous structure prepared by the conventional post-treatment process was not observed in the TEM images obtained after cycling. During cycling, the nanofibers produced by the nanoscale Kirkendall diffusion process exhibited superior electrical properties owing to their superior structural stability because of the unique structure of the hollow or yolk–shell-structured nanospheres.

3. Conclusion

The nanoscale Kirkendall diffusion process was successfully applied to the preparation of nanofibers comprising Sn@void@SnO/SnO_2 yolk–shell nanospheres and hollow SnO/SnO_2 and SnO_2 nanospheres by the electrospinning process. The nanofibers with a unique structure consisting of Sn@void@SnO/SnO_2 yolk–shell nanospheres were prepared at a low oxidation temperature. The complete conversion of the metallic Sn nanopowders embedded within the carbon nanofibers into SnO_2 via the nanoscale Kirkendall diffusion process produced nanofibers with hollow SnO_2 nanospheres. The morphologies and crystal structures of the nanopowders within the nanofibers formed by the nanoscale Kirkendall diffusion process could be easily controlled by changing the post-treatment conditions such as the temperatures and operation times for the reduction and oxidation processes. Therefore, tin-based nanofibers exhibiting a unique structure with various compositions and morphologies could be prepared for a wide range of applications, including energy storage.

4. Experimental Section

Sample Preparation: Tin 2-ethylhexanoate-polyvinylpyrrolidone ($Sn(Oct)_2$–PVP) composite nanofibers were prepared by an electrospinning process. The precursor solution for the electrospinning process was prepared by dissolving 4.8 g of $Sn(Oct)_2$ and 5 g of PVP (M_w: 40 000) in a solution of 40 mL of ethanol and 10 mL of acetic acid. This solution was vigorously stirred overnight. The prepared solution was loaded at a flow rate of 1 mL h^{-1} into a plastic syringe equipped with a 25-gauge stainless steel nozzle. The solution was subsequently ejected and electrospun onto a drum collector covered with an aluminum foil. During the electrospinning process, the distance between the tip and the collector was maintained at 15 cm and the rotation of the drum was maintained at 100 rpm. The applied voltage between the collector and the syringe tip was 15 kV. The resultant $Sn(Oct)_2$–PVP composite nanofibers were stabilized at 180 °C for 1 h in an air atmosphere. For the SnO_2 nanofibers consisting of hollow nanospheres, the post-treatment was conducted at 400 °C for 3 h in the presence of a gas mixture of 10% H_2/Ar. Subsequent treatments were conducted at 400 °C, 500 °C, and 600 °C for 2 h in air. For simplicity, the SnO_2 nanofibers composed of hollow nanospheres formed by the heat treatments at 400 °C, 500 °C, and 600 °C are referred to as "Kirkendall-400," "Kirkendall-500," and "Kirkendall-600" nanofibers, respectively. For comparison, a sample was prepared by producing porous SnO_2 nanofibers without carbon. The direct post-treatment of the $Sn(Oct)_2$–PVP nanofibers at 500 °C for 2 h under an air atmosphere produced the porous-structured SnO_2 nanofibers.

Characterization Techniques: The microstructures of the nanofibers were observed by field-emission scanning electron microscopy (FE-SEM, Hitachi, S-4800) and field-emission transmission electron microscopy (FE-TEM, JEOL, JEM-2100F). In addition, their crystal phases were evaluated by X-ray diffractometry (XRD, X'Pert PRO MPD) using Cu K_α radiation ($\lambda = 1.5418$ Å) at the Korea Basic Science Institute (Daegu). The structure characterization of the carbon in the specimen was performed by Raman spectroscopy (Jobin Yvon LabRam HR800, excited by 632.8 nm He–Ne laser) at room temperature. The surface areas of the nanofibers were measured using the BET method using N_2 as the adsorbate gas. The TG analyses were performed using Pyris 1 TGA (Perkin Elmer) within the temperature range 25 °C–650 °C at a heating rate of 10 °C min^{-1} under a static air atmosphere. An image analyzer (ImageJ, NIH) was used to determine the particle size of the nanospheres.

Electrochemical Measurements: The electrochemical properties of the nanofibers were analyzed by constructing a 2032-type coin cell. The anode was prepared by mixing the active material, carbon black, and sodium carboxymethyl cellulose (CMC) at a weight ratio of 7:2:1. Li metal and microporous polypropylene film were used as the counter electrode and the separator, respectively. The electrolyte consisted of 1 M $LiPF_6$ dissolved in a mixture of ethylene carbonate/dimethyl carbonate (EC/DMC; 1:1 v/v). The discharge/charge characteristics of the samples were investigated by cycling within the 0.01–1.2 V potential range at various current densities. The CVs were measured at a scan rate of 0.1 mV s^{-1}.

Supporting Information

Supporting Information is available from the Wiley Online Library or from the author.

Acknowledgements

This work was supported by the Energy Efficiency & Resources Core Technology Program of the Korea Institute of Energy Technology Evaluation and Planning (KETEP), granted financial resource from the Ministry of Trade, Industry & Energy, Republic of Korea (201320200000420).

[1] J. Wang, N. Du, H. Zhang, J. Yu, D. Yang, *J. Phys. Chem. C* **2011**, *115*, 11302.
[2] Y. Wang, H. C. Zeng, J. Y. Lee, *Adv. Mater.* **2006**, *18*, 645.
[3] J. Ye, H. Zhang, R. Yang, X. Li, L. Qi, *Small* **2010**, *6*, 296.
[4] J. Wu, D. Zeng, X. Wang, L. Zeng, Q. Huang, G. Tang, C. Xie, *Langmuir* **2014**, *30*, 11183.
[5] W. S. Kim, B. S. Lee, D. H. Kim, H. C. Kim, W. R. Yu, S. H. Hong, *Nanotechnology* **2010**, *21*, 245605.
[6] W. J. Lee, M. H. Park, Y. Wang, J. Y. Lee, J. Cho, *Chem. Commun.* **2010**, *46*, 622.
[7] J. Cao, T. Zhang, F. Li, H. Yang, S. Liu, *New J. Chem.* **2013**, *37*, 2031.
[8] H. Kim, J. Cho, *J. Mater. Chem.* **2008**, *18*, 771.
[9] M. S. Park, G. X. Wang, Y. M. Kang, D. Wexler, S. X. Dou, H. K. Liu, *Angew. Chem.* **2007**, *119*, 764.
[10] C. Guan, X. Wang, Q. Zhang, Z. Fan, H. Zhang, H. J. Fan, *Nano Lett.* **2014**, *14*, 4852.
[11] N. G. Cho, D. J. Yang, M. J. Jin, H. G. Kim, H. L. Tuller, I. D. Kim, *Sens. Actuators B Chem.* **2011**, *160*, 1468.
[12] Y. J. Hong, J. W. Yoon, J. H. Lee, Y. C. Kang, *Chem. Eur. J* **2015**, *21*, 371.
[13] R. Liu, S. Yang, F. Wang, X. Lu, Z. Yang, B. Ding, *ACS Appl. Mater. Interfaces* **2012**, *4*, 1537.
[14] J. Liang, X. Y. Yu, H. Zhou, H. B. Wu, S. Ding, X. W. D. Lou, *Angew. Chem.* **2014**, *53*, 12803.
[15] Y. N. Ko, S. B. Park, Y. C. Kang, *Small* **2014**, *10*, 3240.
[16] J. K. Choi, I. S. Hwang, S. J. Kim, J. S. Park, S. S. Park, U. Jeong, Y. C. Kang, J. H. Lee, *Sens. Actuators B Chem.* **2010**, *150*, 191.
[17] Y. E. Chang, D. Y. Youn, G. Ankonina, D. J. Yang, H. G. Kim, A. Rothschild, I. D. Kim, *Chem. Commun.* **2009**, *27*, 4019.
[18] Z. Wang, D. Luan, F. Y. C. Boey, X. W. Lou, *J. Am. Chem. Soc.* **2011**, *133*, 4738.
[19] Y. J. Hong, M. Y. Son, Y. C. Kang, *Adv. Mater.* **2013**, *25*, 2279.
[20] Y. J. Hong, Y. C. Kang, *Small* **2015**, *11*, 2157.
[21] H. Wang, A. L. Rogach, *Chem. Mater.* **2013**, *26*, 123.
[22] Z. Wen, Q. Wang, Q. Zhang, J. Li, *Adv. Funct. Mater.* **2007**, *17*, 2772.
[23] H. S. Oh, H. N. Nong, P. Strasser, *Adv. Funct. Mater.* **2015**, *25*, 1074.
[24] R. Yang, Y. Gu, Y. Li, J. Zheng, X. Li, *Acta Mater.* **2010**, *58*, 866.
[25] J. Shin, S. J. Choi, I. Lee, D. Y. Youn, C. O. Park, J. H. Lee, H. L. Tuller, I. D. Kim, *Adv. Funct. Mater.* **2013**, *23*, 2342.
[26] Z. Chen, M. Zhou, Y. Cao, X. Ai, H. Yang, J. Liu, *Adv. Energy Mater.* **2012**, *2*, 94.
[27] K. Kravchyk, L. Protesescu, M. I. Bodnarchuk, F. Krumeich, M. Yarema, M. Walter, C. Guntlin, M. V. Kovalenko, *J. Am. Chem. Soc.* **2013**, *135*, 4199.
[28] M. Li, Q. Lu, Y. Nuli, X. Qian, *Electrochem. Solid State Lett.* **2007**, *10*, K33.
[29] X. W. Lou, C. M. Li, L. A. Archer, *Adv. Mater.* **2009**, *21*, 2536.
[30] J. S. Chen, L. A. Archer, X. W. Lou, *J. Mater. Chem.* **2011**, *21*, 9912.
[31] X. M. Yin, C. C. Li, M. Zhang, Q. Y. Hao, S. Liu, L. B. Chen, T. H. Wang, *J. Phys. Chem. C* **2010**, *114*, 8084.
[32] W. S. Kim, Y. Hwa, J. H. Jeun, H. J. Sohn, S. H. Hong, *J. Power Sources* **2013**, *225*, 108.
[33] P. Wu, N. Du, H. Zhang, C. Zhai, D. Yang, *ACS Appl. Mater. Interfaces* **2011**, *3*, 1946.
[34] L. Xiao, J. Li, Q. Li, L. Zhang, *J. Solid State Electrochem.* **2010**, *14*, 931.
[35] H. X. Yang, J. F. Qian, Z. X. Chen, X. P. Ai, Y. L. Cao, *J. Phys. Chem. C* **2007**, *111*, 14067.
[36] R. Liu, N. Li, D. Li, G. Xia, Y. Zhu, S. Yu, C. Wang, *Mater. Lett.* **2012**, *73*, 1.
[37] H. J. Fan, U. Gösele, M. Zacharias, *Small* **2007**, *3*, 1660.
[38] M. Knez, R. Scholz, K. Nielsch, E. Pippel, D. Hesse, M. Zacharias, U. Gösele, *Nat. Mater.* **2006**, *5*, 627.
[39] S. H. Choi, J. K. Lee, Y. C. Kang, **2015**, *8*, 1584.
[40] Y. Dong, Z. Zhao, Z. Wang, Y. Liu, X. Wang, J. Qiu, *ACS Appl. Mater. Interfaces* **2015**, *7*, 2444.
[41] H. El-Shinawi, A. S. Schulze, M. Neumeier, T. Leichtweiß, J. Janek, *J. Phys. Chem. C* **2014**, *118*, 8818.
[42] Y. Sharma, N. Sharma, G. V. Subba Rao, B. V. R. Chowdari, *Chem. Mater.* **2008**, *20*, 6829.
[43] N. Li, G. Liu, C. Zhen, F. Li, L. Zhang, H. M. Cheng, *Adv. Funct. Mater.* **2011**, *21*, 1717.
[44] S. M. Lee, S. H. Choi, Y. C. Kang, *Chem. -Eur. J.* **2014**, *20*, 15203.

Received: April 6, 2015
Revised: May 13, 2015
Published online: June 8, 2015

